



# Novel utilization of liquid feedstock in high velocity air fuel (HVOF) spraying to deposit solid lubricant reinforced wear resistant coatings

Ashish Ganvir<sup>a,\*</sup>, Adwait Rajeev Jahagirdar<sup>b</sup>, Antonio Mulone<sup>c</sup>, Louise Örnfeldt<sup>c</sup>, Stefan Björklund<sup>b</sup>, Uta Klement<sup>c</sup>, Shrikant Joshi<sup>b</sup>

<sup>a</sup> University of Turku, FI-20014, Finland

<sup>b</sup> University West, 46186, Trollhättan, Sweden

<sup>c</sup> Chalmers University of Technology, Gothenburg, Sweden

## ARTICLE INFO

Associate Editor: Yip-Wah Chung

### Keywords:

Hybrid  
Wear  
HVOF  
Coatings  
Suspension  
Boron nitride

## ABSTRACT

The ability to axially inject liquid feedstock has encouraged the thermal spray research community to explore this concept to deposit coatings for various next generation functional applications. The current study explores the utilization of liquid feedstock in high velocity air fuel (HVOF) spraying to deposit solid lubricant reinforced wear resistant coatings for the first time. The study successfully demonstrates the use of a powder-suspension hybrid processing approach to incorporate a solid lubricant Boron Nitride (as suspension) in a wear resistant  $\text{Cr}_3\text{C}_2\text{-NiCr}$  (as powder) cermet matrix. Coatings were characterized using Scanning Electron Microscopy and Raman Spectroscopy to analyze their microstructure and phase constitution. The results show that the tribological performance of the hexagonal boron nitride (hBN)-incorporated composite coating was significantly better than the traditional powder-derived  $\text{Cr}_3\text{C}_2\text{-NiCr}$  coating. Such hBN-incorporated composite coatings are needed to improve the mechanical properties and enhance the overall tribological performance of metallic components used in various applications, especially at high temperature such as cylinder bore, pistons, deformation tools, etc. The limitations of liquid based lubricants at high temperature motivates the use of hBN reinforced composite coatings as it can form a protective solid lubrication tribo-film. The study concludes that the emerging HVOF technology can accommodate liquid feedstock and be successfully utilized to deposit hybrid powder-suspension composite coatings to create multi length scale microstructures which can be attractive for combining different tribological attributes in the same coatings system.

## 1. Introduction

Failure of engineering components subjected to tribological conditions has been a critical issue for the mechanical industries. To minimize the cost of repair or replacement, improvement in the tribological properties, especially wear resistance, are required. Wear-resistant coatings are commonly applied on the surface of the components to tailor the coefficient of friction (CoF) (Motru et al., 2020) and protect the surface from wear (Xiong et al., 2020). (Hoornaert et al., 2010) described in their review paper that over the years, various wear-resistant coating materials (nitrides, carbides, borides, etc.) and their processing routes (chemical vapour deposition (CVD), physical vapour deposition (PVD), thermal spraying, etc.) have been developed. But the ability to deposit coatings over large areas in a shorter time has

given thermal spray an extra edge over other coating technologies such as the ones mentioned above. The most widely used thermal spray techniques for producing wear resistant coatings are high velocity oxy fuel (HVOF) (Wang et al., 2020) and plasma spray (Umanskii et al., 2020) where a coarse powder feedstock is injected into the heat source (combustion flame/plasma plume) to produce dense wear resistant coatings. For example in case of HVOF, (Guo et al., 2014) studied the influence of particle velocity and temperature on the microstructure and hardness of WC-CoCr coatings, whereas (Lima et al., 2020) successfully processed cobalt-chrome alloys via HVOF to produce wear resistant coatings which showed an higher resistance to abrasive wear as compared to WC-CoCr obtained by gas tungsten arc welding hot-wire cladding. Similarly, in case of plasma spray (Du et al., 2011) studied the wear performance of  $\text{NiCr/Cr}_3\text{C}_2\text{-NiCr}$ /hexagonal boron nitride

\* Corresponding author.

E-mail addresses: [ashish.ganvir@utu.fi](mailto:ashish.ganvir@utu.fi) (A. Ganvir), [adwait.jahagirdar@student.hv.se](mailto:adwait.jahagirdar@student.hv.se) (A.R. Jahagirdar), [mulone@chalmers.se](mailto:mulone@chalmers.se) (A. Mulone), [louiseornfeldt@gmail.com](mailto:louiseornfeldt@gmail.com) (L. Örnfeldt), [Stefan.bjorklund@hv.se](mailto:Stefan.bjorklund@hv.se) (S. Björklund), [uta.klement@chalmers.se](mailto:uta.klement@chalmers.se) (U. Klement), [shrikant.joshi@hv.se](mailto:shrikant.joshi@hv.se) (S. Joshi).

<https://doi.org/10.1016/j.jmatprotec.2021.117203>

Received 4 November 2020; Received in revised form 17 April 2021; Accepted 2 May 2021

Available online 6 May 2021

0924-0136/© 2021 The Author(s). Published by Elsevier B.V. This is an open access article under the CC BY license (<http://creativecommons.org/licenses/by/4.0/>).

(hBN) plasma sprayed composite coating and showed a significant decrease in the friction coefficient due to the presence of hBN whereas (Forn et al., 2003) studied the mechanical and tribological properties of plasma sprayed Al–Si–Mo coatings and found that the increase of Mo content in the coating is beneficial for the mechanical properties.

A more recent addition to the thermal spray technologies is high velocity air fuel (HVOF) spraying which has relatively lower processing temperature, but higher kinetic energy compared to HVOF and plasma spray. The ability to spray colder and faster makes HVOF more promising to deposit materials which are prone to in-flight oxidation at higher temperatures such as WC–Co (Varis et al., 2020), NiCrMoNb–Cr<sub>3</sub>C<sub>2</sub> (Matikainen et al., 2017a), Cr<sub>3</sub>C<sub>2</sub>–NiCr (Janka et al., 2017) etc. Cr<sub>3</sub>C<sub>2</sub>–NiCr is considered to be the most promising wear resistant material, especially for high temperature applications, due to its high corrosion resistance and impressive wear resistant properties at both room as well as high temperatures as shown by (Guilemany et al., 2002) and (Matthews et al., 2009). The benefits Cr<sub>3</sub>C<sub>2</sub>–NiCr as a wear resistant coating material was realized by (Chhabra and Kaur, 2020) who demonstrated an increase in wear resistance of as-deposited coatings at all test parameters as well as (Liu et al., 2020) who showed the tribological performance at room as well as high temperature can be further enhanced by annealing the as-deposited coatings at 600 °C in air. However, (Lu et al., 2020) showed that it is extremely important to produce pore-free Cr<sub>3</sub>C<sub>2</sub>–NiCr coatings as the presence of porosity can deteriorate the overall tribological performance of the coating. The Cr<sub>3</sub>C<sub>2</sub>–NiCr wear resistant coatings processed via more traditional thermal spray techniques such as plasma spray and HVOF as shown by (Espallargas et al., 2008) and (Zhang and Hou, 2013), respectively have been used in numerous applications including engine cylinder bore, pistons, steam turbine blades, boiler tubes, deformation tools, etc. However, as demonstrated by (Janka et al., 2017) the risk of higher porosity, in-flight oxidation and carbide decomposition or carbide-matrix dissolution due to the excessive heat and low kinetic energy in either HVOF or plasma spray is encouraging the thermal spray community to use HVOF.

In applications where two components slide against each other, the state-of-the-art cost-effective lubricants, oils and greases are introduced in-between the surfaces in contact to reduce the coefficient of friction (CoF). However, these liquid lubricants tend to lose their integrity when working at extreme conditions such as vacuum environment, high temperature or very high contact pressure as mentioned by (Donnet and Erdemir, 2004) in their review on conventional and emerging lubricants. An alternative approach to address these problems as demonstrated by (Espallargas and Armada, 2015) is to use solid lubricants. Unlike the liquid lubricants, the solid lubricants are mixed with the base material and are processed together to form coatings. The solid lubricant particles then get embedded in the base material's matrix. During application, solid lubricants form a thin lubricating film in-between the friction surfaces. Commonly used solid lubricants are the compounds of fluorides (CaF<sub>2</sub>, BaF<sub>2</sub>, etc.) & metal disulphides (MoS<sub>2</sub>, TaS<sub>2</sub>, etc.) as demonstrated by (Huang et al., 2009) as well as (Zhang et al., 2009). Moreover use of metal oxides (B<sub>2</sub>O<sub>3</sub>, MoO<sub>3</sub>, ZnO, TiO<sub>2</sub>, etc.) and soft noble metals (Au, Ag, etc.) were also demonstrated in literature by (Kerkwijk et al., 2004) and (Shtansky et al., 2013), respectively.

However, most of the above-mentioned solid lubricants have limited working abilities at different working conditions. Considering these limitations, as pointed out by (Chkhartishvili et al., 2016) in their review, hBN stands out of most of the available solid lubricants due to its good thermal stability, good heat conductivity, low density and low coefficient of friction at higher temperatures. hBN has a crystalline lamellar structure, in which the inter-molecular bonding is strong, but the inter-layer bonding is by weak van der Waals forces. Thus, when hBN is present at the sliding interface, the atomic layers of hBN which are aligned parallel to the sliding motion, shear with ease and give rise to the levels of low friction as demonstrated by (Tsunekawa et al., 2006). It has been shown by (Cao, 2016), (Tsunekawa et al., 2006) as well as (Zhu

et al., 2019) that with the addition of hBN as a solid lubricant, CoF can be lowered and in turn further improve the wear resistance of the thermally sprayed coatings. However, in these studies hBN was processed using the traditional feeding and spraying method where a composite feedstock was prepared by pre-mixing the hBN powder with the metallic/ceramic/cermet powder, ball-milled and spray dried prior to spraying.

Nevertheless, the pre-processing of hBN with other powder materials to facilitate the deposition of composite coatings is of course time consuming as well as expensive. Therefore, the authors have demonstrated for the first time a neat way of processing hBN reinforced composite coatings using a so called 'hybrid thermal spray' where two or more feedstock materials can be introduced simultaneously or sequentially into the combustion flame/plasma plume to produce composite coatings. Moreover, hybrid thermal spray also provides benefits in terms of tailoring the coating architectures by enabling an independent control on feeding of different feedstock materials. The hybrid processing is not only limited to powder feedstocks but a combination of powder as well as liquid (e.g. suspension/solution precursor) materials can also be utilized to create multilength scale microstructures which was successfully demonstrated by (Björklund et al., 2018). So far, the hybrid processing approach has only been utilized for plasma spraying (Björklund et al., 2018) and HVOF spraying (Kiilakoski et al., 2019), however this work has successfully extended the use of hybrid processing route to the newly emerging HVOF technique.

Therefore, the current study shows the hybrid processing using HVOF technique where a solid lubricant (hBN) was fed in the form of suspension simultaneously with the wear resistant Cr<sub>3</sub>C<sub>2</sub>–NiCr powder to create a multi length scale microstructure wear resistant composite coating. A traditional powder-derived Cr<sub>3</sub>C<sub>2</sub>–NiCr powder was also deposited under similar processing conditions as a reference wear resistant coating. Both the composite as well as the traditional powder-derived coatings were exposed to a sliding wear test. Mechanical properties such as hardness and fracture toughness were also determined. Furthermore, the coatings were also characterized using Scanning Electron Microscopy and Raman Spectroscopy to analyze their microstructure and phases.

## 2. Materials and methods

### 2.1. Feedstock preparation

The feedstock materials used in this study were commercially available Amperit® 588.059 Cr<sub>3</sub>C<sub>2</sub>–NiCr (75–25) powder (Höganäs AB, Sweden) and HeBoCoat® PL-W 310 hBN (Henze Boron Nitride Products AG, Germany) suspension. The suspension obtained from the supplier was highly solid loaded (31 %) in water as well as extremely viscous. Therefore, prior to spraying, the suspension was diluted with water to a solid loading of 15 wt.% to facilitate the easy feeding of the suspension. The mean particle size of hBN solute particles in the suspension as per the manufacturer was of about 2–5 µm whereas the mean particle size of the Cr<sub>3</sub>C<sub>2</sub>–NiCr powder was about 18–24 µm.

### 2.2. Coating deposition

The substrate material used in this study was SSAB Domex® 350LA (low-alloyed steel, SSAB AB) in form of ø25 mm round coupons. Prior to the coating deposition, all the substrates were grit blasted using alumina powder (220 grit size) to approximately 3 µm (Ra) surface roughness. The surface roughness was measured using a MITUTOYO SURFTTEST-301 (Mitutoyo, Takatsu-ku, Kawasaki, Japan) profilometer. Coatings were sprayed using a HVOF spray system (Uniquelcoat, Richmond, USA) with novel in-house made dual feedstock arrangement as shown in Fig. 1. About 200 µm thick hybrid powder-suspension composite coating was deposited along with a traditional powder-derived powder (Cr<sub>3</sub>C<sub>2</sub>–NiCr) coating of about the same thickness. Both the hybrid as

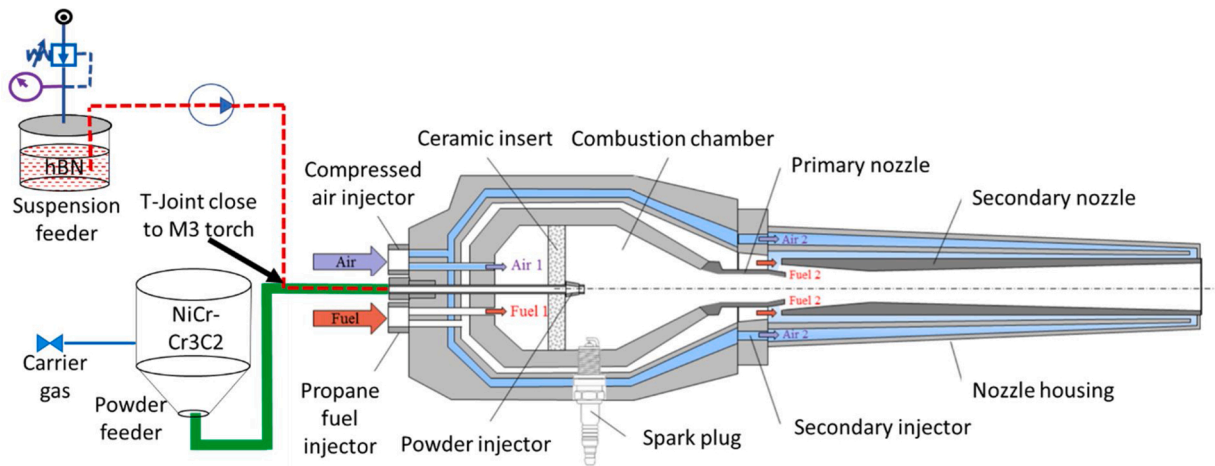


Fig. 1. Arrangement to introduce dual feedstock in an HVOF system.

well as the traditional powder-derived coating was sprayed using exactly the same HVOF spray parameters where the spray distance, air pressure, nitrogen carrier gas flow and surface speed were 350 mm, 111 psi, 40 L/min, and 100 m/min, respectively. The feed rate for  $\text{Cr}_3\text{C}_2$ -NiCr powder in both the traditional powder-derived as well as the hybrid coating was 75 g/min whereas the hBN suspension feed rate to deposit the hybrid coating was 50 mL/min.

### 2.3. Coating characterization

To characterize the morphology and microstructure of feedstocks as well as coatings, microscopy was performed using a TM3000 Tabletop Scanning Electron Microscope (SEM) (HITACHI, Tokyo, Japan), a Philips XL30 ESEM (Philips/Fei, Eindhoven, The Netherlands/ Hillsboro, USA) and a Zeiss Gemini SEM 450 (Zeiss, Oberkochen, Germany). To prepare the cross-sections of the coatings, the coupons were cut, ground, mounted and mirror polished. The mounting and polishing of the specimens were done in a Struers CitoPress-20 and TegraPol-31/ Tegraforce-5 machines, respectively. Area fraction of porosity was calculated using image analysis technique where 10 SEM micrographs at 1000-times magnification were randomly captured across the cross-section of the coating. The image analysis was done using the public domain Java based image processing software ImageJ (Fiji) (ImageJ Software, 2021). SEM images were converted from grey scale to binary and a relative area fraction of the porosity was then reported as an average of the 10 images with appropriate standard deviation. More details about the image analysis can be found in earlier work (Ganvir, 2016; Ganvir et al., 2018). Raman spectra were acquired using a WITec alpha300 R confocal Raman microscope (WITec, Germany) using a laser source of 532 nm. The measurements were performed using 50x and 100x objectives, a 300  $\mu\text{m}$  confocal pinhole and a 600 lines/mm rotatable diffraction grating. The Raman spectra were collected with an acquisition time of 10 s and repeated once in order to remove peaks due to cosmic rays.

### 2.4. Mechanical testing

Hardness of the coatings was measured using a Vickers indenter (Shimadzu HMV-2 T Microhardness Tester). A total of 10 indents were made on as-sprayed polished cross-sections with a maximum load of 1 N (HV0.1) and the average values of the hardness was determined. The same Vickers indenter was used to introduce cracks without significantly damaging the coating at a maximum load of 30 N, for a dwell time of 15 s. A total of 10 indents were made across the mirror polished cross-section. SEM images for all the indents were captured to measure the crack length ( $c$ ) and the indent half-diagonal length ( $a$ ). The fracture

toughness was then calculated using Evans and Wilshaw's Eq. (1) (Evans and Wilshaw, 1976) as given below:

$$K_{IC} = 0.079 \left( \frac{P}{a^{1.5}} \right) \log \left( 4.5 \frac{a}{c} \right) \quad (1)$$

Where,  $K_{IC}$  is the mode I indentation fracture toughness ( $\text{MPa}\cdot\text{m}^{1/2}$ ),  $P$  is the indentation load (N),  $a$  is the indentation half-diagonal length (m) and  $c$  is the crack length (m).

### 2.5. Sliding wear test

The as-sprayed coatings were polished to a surface roughness of ( $R_a$ )  $< 0.2 \mu\text{m}$  prior to the sliding wear test which was performed as per ASTM G99 standard (ASTM G99, 2021). The test was done on  $\phi 25$  mm mirror polished coupons by employing an  $\text{Al}_2\text{O}_3$  ball of diameter 6 mm, at a load of 15 N sliding against a disc rotated at 0.2 m/s velocity for a total sliding distance of 2500 m. After the wear test, the weight loss was measured using a high accuracy weighing balance (Sartorius, Cubis® II, Sartorius GmbH, Göttingen, Germany) with an accuracy of 0.1 mg. Three different wear tracks of 5 mm, 7 mm, and 9 mm radius were made on each coupon. On each of the three wear tracks, three different locations were randomly selected to measure the local volume loss using White Light Interferometry (WLI) (Profilm 3D, Filmetrics Europe GmbH, Germany). The local area loss was then calculated as the ratio of the local volume loss and the length of the local region. An average of the three local area losses was calculated and multiplied to the perimeter of the respective wear tracks at each radius (5 mm, 7 mm, and 9 mm) to obtain the total volume loss for the respective wear tracks. The specific wear rate for each wear track was then calculated using Eq. (2) as shown below and the average specific wear rate of all three wear tracks is reported.

$$\text{Wear rate} \left( \frac{\text{mm}^3}{\text{Nm}} \right) = \frac{\text{Total volume loss of the wear track}}{\text{Force} * \text{distance}} \quad (2)$$

## 3. Results & discussion

### 3.1. Microstructure

#### 3.1.1. Feedstock

Fig. 2 shows the SEM micrographs of both the  $\text{Cr}_3\text{C}_2$ -NiCr powder (a) and hBN dried suspension (b) feedstocks. An agglomerated and sintered, nearly spherical morphology of  $\text{Cr}_3\text{C}_2$ -NiCr cermet powder is evident from Fig. 2(a) where the non-spherical grey particles (solid arrow) are the  $\text{Cr}_3\text{C}_2$  particles which are bound together in a white NiCr metal matrix (dashed arrows). The size of the  $\text{Cr}_3\text{C}_2$ -NiCr cermet powder



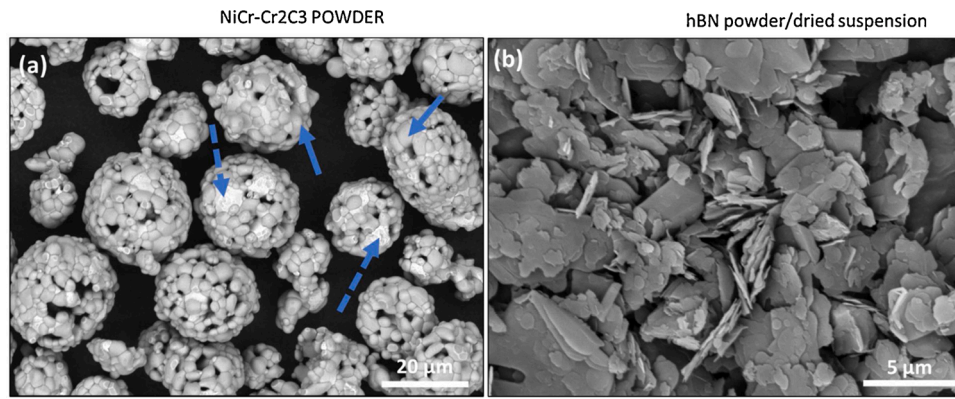


Fig. 2. SEM micrographs showing the morphology of feedstocks (a) Cr<sub>3</sub>C<sub>2</sub>-NiCr powder and (b) hBN dried suspension.

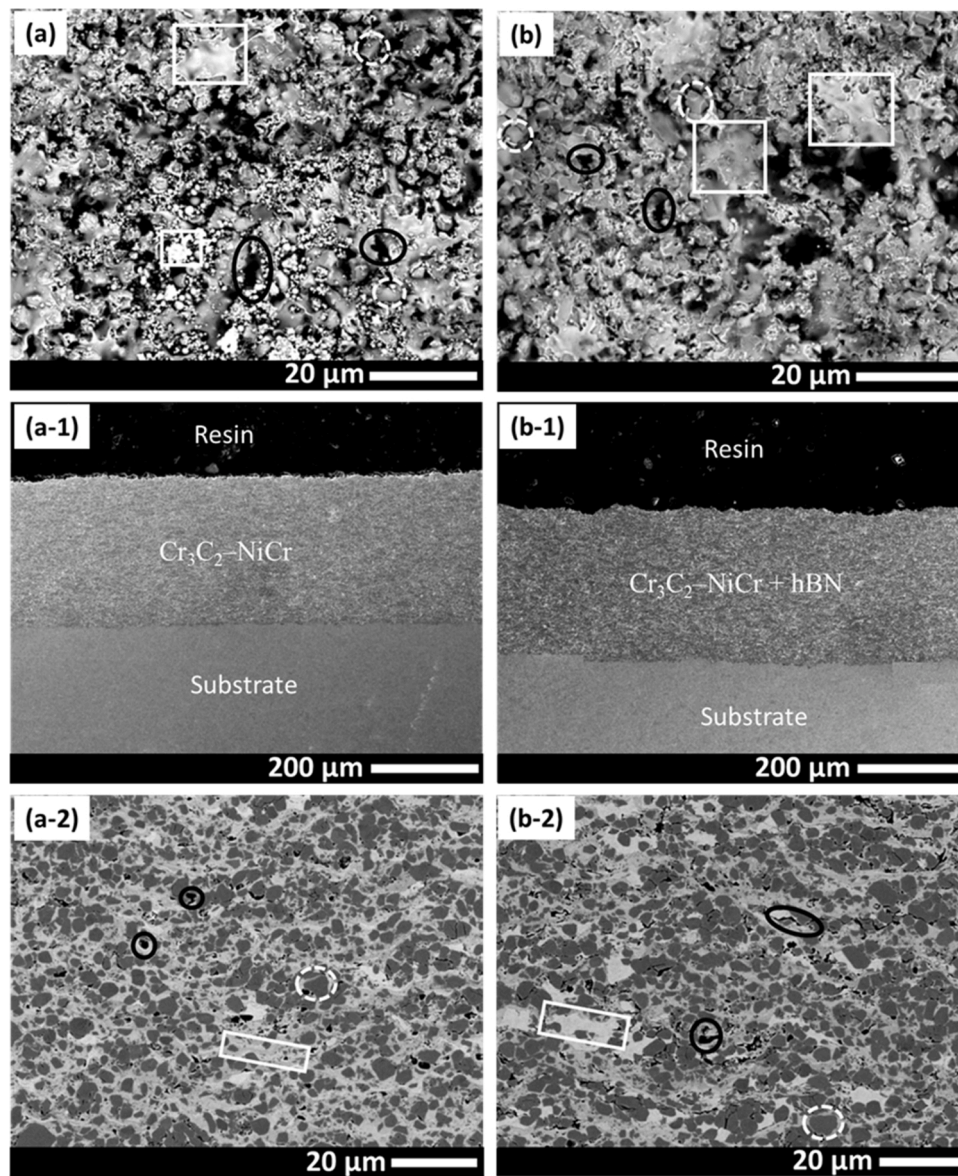


Fig. 3. SEM micrographs of the top-surface (a and b), polished cross-section (a-1 and b-1) at low magnification and at high magnification (a-2 and b-2) for traditional powder-derived & composite coatings, respectively. The various microstructural features are marked with white dotted circle (ceramic carbide particles), white square/rectangle (metal matrix) and black circle/ellipse (pores & cracks).



particles is about 15–25  $\mu\text{m}$ , which consist of  $\text{Cr}_3\text{C}_2$  particles of approximately 4–6  $\mu\text{m}$ . Moreover, agglomerated hBN particles with a platelet like morphology can be seen from Fig. 2(b) where a wider size range (<1  $\mu\text{m}$  to about 20  $\mu\text{m}$ ) for hBN particles is evident with some of the platelets clearly revealing its two-dimensional structure. It is important to point out that the SEM micrograph shown in Fig. 2(b) for hBN was captured from the dried concentrated suspension and therefore most of the hBN particles appear as agglomerates of several hBN platelets.

### 3.1.2. Coating

Fig. 3 shows the SEM micrographs of the as-deposited composite as well as traditional powder-derived coating. The top surface of both the coatings showed the presence of ceramic carbide particles (marked with white dotted circles in Fig. 3(a) and (b)) along with the presence of the semi-molten/molten metal matrix splats (marked with the white squares/rectangles) and porosity (marked with the black circles/ellipses). The polished cross-sections of both coatings at lower magnifications show an approximately 200  $\mu\text{m}$  thick uniform coating that adheres well to the substrate (see Fig. 3 (a1) and (b1)). At high magnification, images of the polished cross-sections as shown in Fig. 3(a2) and (b2) reveal more detailed microstructural features such as the dark phase carbide particles (marked with the white dotted circles) embedded in a light grey metal matrix phase (marked with the white squares/rectangles) and porosity (marked with the black circles/ellipses). It is also important to point out that the presence of porosity appears to be higher in the composite coating. The porosity is primarily found at the interface of the metal matrix and the carbide particles. The quantification of the porosity using image analysis is presented in Table 1 which further suggests the presence of higher porosity ( $4.6 \pm 0.2$  %) in the composite coating as compared to the traditional powder-derived coating ( $3.4 \pm 0.3$  %). Another point to be noted here is the difficulty to distinguish the hBN particles from the pores in the coatings due to a similar contrast difference when acquiring SEM images with back scattered electrons. However, as shown in Fig. 4b, the secondary electron (SE) micrograph acquired with an in-lens detector from the cross-section of the composite coating clearly reveals the presence of a fine platelet-like structure. The observed phase can be related to hBN particles, as the same structure is not observed when imaging the traditional powder-derived coating, see Fig. 4c and d. It needs to be mentioned that the bright round particles in Fig. 4b are residues from the polishing media used for the metallographic preparation of the sample.

To further confirm the presence of hBN, EDS as well as Raman analysis was performed on the composite coating and the results are included in the following paragraphs.

### 3.2. EDS analysis

The results of EDS analyses performed on the polished cross-section of the composite coatings are shown in Fig. 5. As seen in the EDS maps in Fig. 5b, B and N-rich areas are observed mainly in three locations (highlighted with number 1, 2 and 3). These locations appear in dark contrast in the backscattered electrons (BSE) image in Fig. 5a. A closer

**Table 1**

Various attributes of the hybrid composite and traditional powder-derived coatings studied in this work (coating thickness, thickness per pass, porosity, hardness & fracture toughness).

Coating ID/ Properties	Coating thickness ( $\mu\text{m}$ )	Coating thickness per pass ( $\mu\text{m}/\text{pass}$ )	Coating Porosity (Area %)	Hardness (HV0.1)	Fracture toughness ( $\text{MPa} \cdot \text{m}^{1/2}$ )
Traditional powder- derived	$289 \pm 05$	9.6	$3.4 \pm 0.3$	$1096 \pm 66$	$5.7 \pm 0.2$
Composite	$309 \pm 07$	6.9	$4.6 \pm 0.2$	$997 \pm 64$	$4.0 \pm 0.4$

examination of these locations reveal that the observed B and N-rich areas are observed where pores are present (see Fig. 5c). To acquire these images, the AsB detector of the Zeiss Gemini SEM 450 was used in TOPO mode, which enables composition and topography imaging.

### 3.3. Phase analysis using RAMAN

To confirm the EDS results and to further prove the presence of hBN within  $\text{Cr}_3\text{C}_2$ -NiCr composite coatings, Raman spectra were acquired from the polished cross-section of the hBN reinforced coating and compared to the spectra acquired from hBN powder. The results are shown in Fig. 6. The measurements were acquired in the highlighted area in Fig. 6a, which is shown at higher magnification in Fig. 6b. The reference spectrum measured from the hBN powder shows the characteristic hBN peak at around  $1367 \text{ cm}^{-1}$ , see Fig. 6c, which can be attributed to the in plane B–N stretching vibrational mode (Göncü et al., 2017). The same peak is observed in the two representative Raman spectra acquired from the regions previously described in Fig. 5. Together with the hBN peak, also a low-intensity peak at around  $1590 \text{ cm}^{-1}$  can be observed, as shown in the Raman spectra acquired from site 2, see Fig. 6c. This peak can be related to the graphitic G band of carbon materials which can be observed in carbon derived from carbides, in this case the  $\text{Cr}_3\text{C}_2$  carbide (Liu et al., 2019; Urbonaite et al., 2008).

### 3.4. Understanding the HVOF hybrid processing route & coating formation

The authors have employed for the first time the powder-suspension hybrid processing approach in HVOF spraying. So far HVOF has only been utilized to process powder feedstock to deposit coatings for various applications (Varis et al., 2020). However, this study demonstrates that it is possible to process a mixture of suspension and powder feedstocks as depicted in Figs. 1 and 7, justifying the term ‘hybrid’. Fig. 7 shows a schematic representation of the novel HVOF hybrid processing route alongside conventional HVOF processing. As can be seen from the schematic, the hBN suspension and  $\text{Cr}_3\text{C}_2$ -NiCr powder feedstocks were fed individually but simultaneously utilizing a T-joint at the rear of the torch. The powder was carried to the injector with 40 L/min nitrogen as carrier gas whereas the suspension was pumped as a stream towards the T-joint at a 100 mL/min feed rate by a liquid feed system where it was atomized into droplets by the carrier gas as it entered the injector tube after existing the orifice of the T-joint. Therefore, as shown in the schematic, the 100 mm long injector tube consisted of a mix of suspension droplets (i.e., water & hBN platelets) and  $\text{Cr}_3\text{C}_2$ -NiCr powder particles carried by nitrogen gas. At the exit of the injector, the suspension droplets were further atomized into even finer droplets due to the drag from the coaxial air flow around the injector tip which is used to cool-down the injector. The gradual increase of the combustion gas velocity in the combustion chamber, which starts at approximately 50 m/s at the ceramic insert, increases to approximately 800 m/s at the primary nozzle and can reach up to 1400 m/s–1500 m/s at the secondary nozzle, continuously atomizes the suspension droplets into further finer droplets (not depicted to scale in the schematic in Fig. 7). The  $\text{Cr}_3\text{C}_2$ -NiCr powder particles exiting the injector can also have some moisture on their surface due to the shared transport with the suspension droplets through the injector. The existence of suspension droplets and wet powder particles at the exit of the injector is termed as *stage I*.

The break-up of the suspension droplets has been studied in detail by the authors in earlier work on plasma spraying (Ganvir et al., 2019) wherein the carrier gas and plasma plume were shown to be responsible for a larger initial droplet breaking up into fine suspension droplets. Similarly, in this study, it can be said that the carrier gas (nitrogen), the coaxial air flow and the supersonic flame with a velocity of more than 1000 m/s (Verstak and Kusinski, 2012) were responsible for breaking up the suspension stream into fine droplets.

After exiting the injector, the hBN suspension droplets as well as the

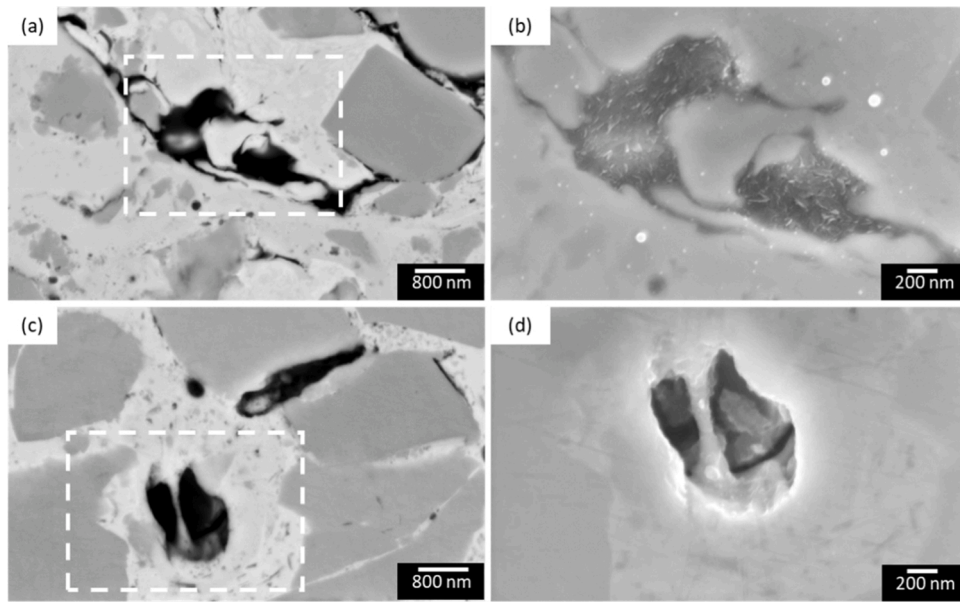


**Fig. 4.** BSE and SE micrographs of the cross-section of the composite coating (a and b) and of the powder-derived coating (c and d). The dashed box in (a) and (c) highlights the area from where the SE micrographs (b) and (d) are acquired.

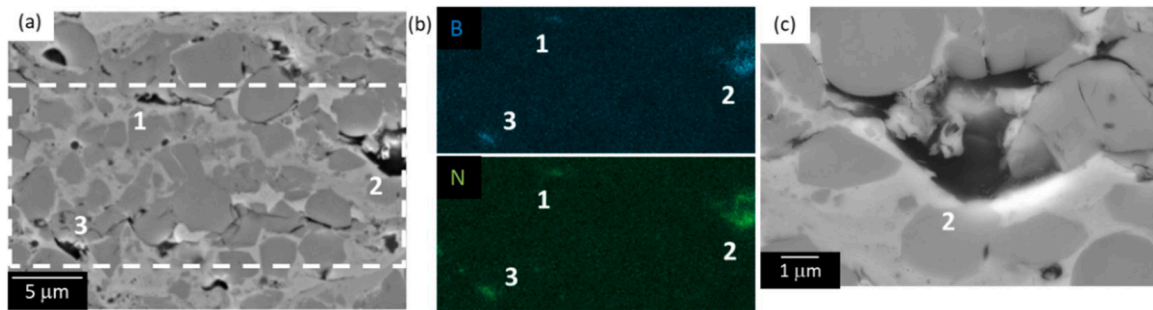


**Fig. 5.** BSE micrographs (a and c) of the polished cross-section of the composite coating, overview and at higher magnification, respectively, and EDS maps (b) showing the distribution of B and N at the three (1, 2 & 3) locations illustrated in (a).

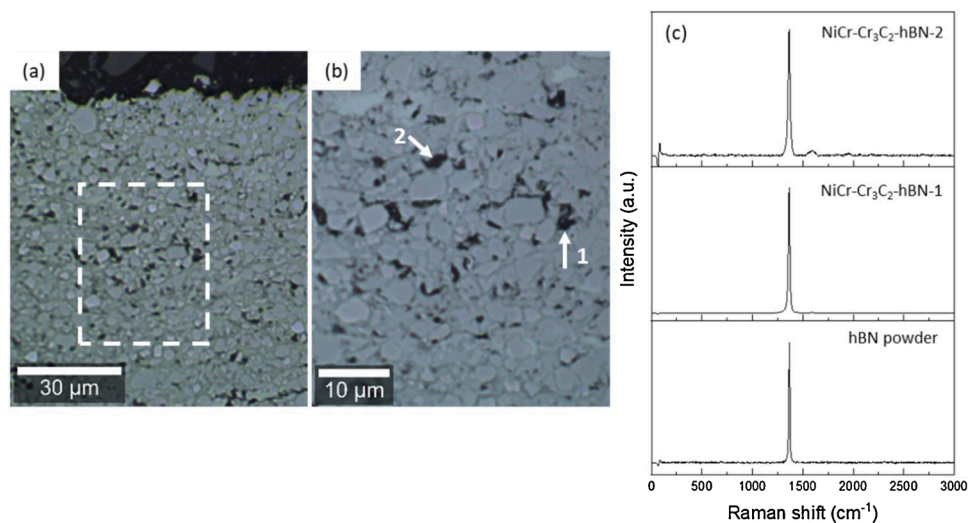


**Fig. 6.** Optical micrographs of the polished cross-section of the composite coating (a and b) and Raman spectra acquired from the hBN powder and from the composite cross-section (c). The dashed box in (a) highlights the area used for Raman analysis, which is shown at higher magnification in (b). The numbers 1 and 2 in (b) points out the locations where the Raman spectra were acquired.

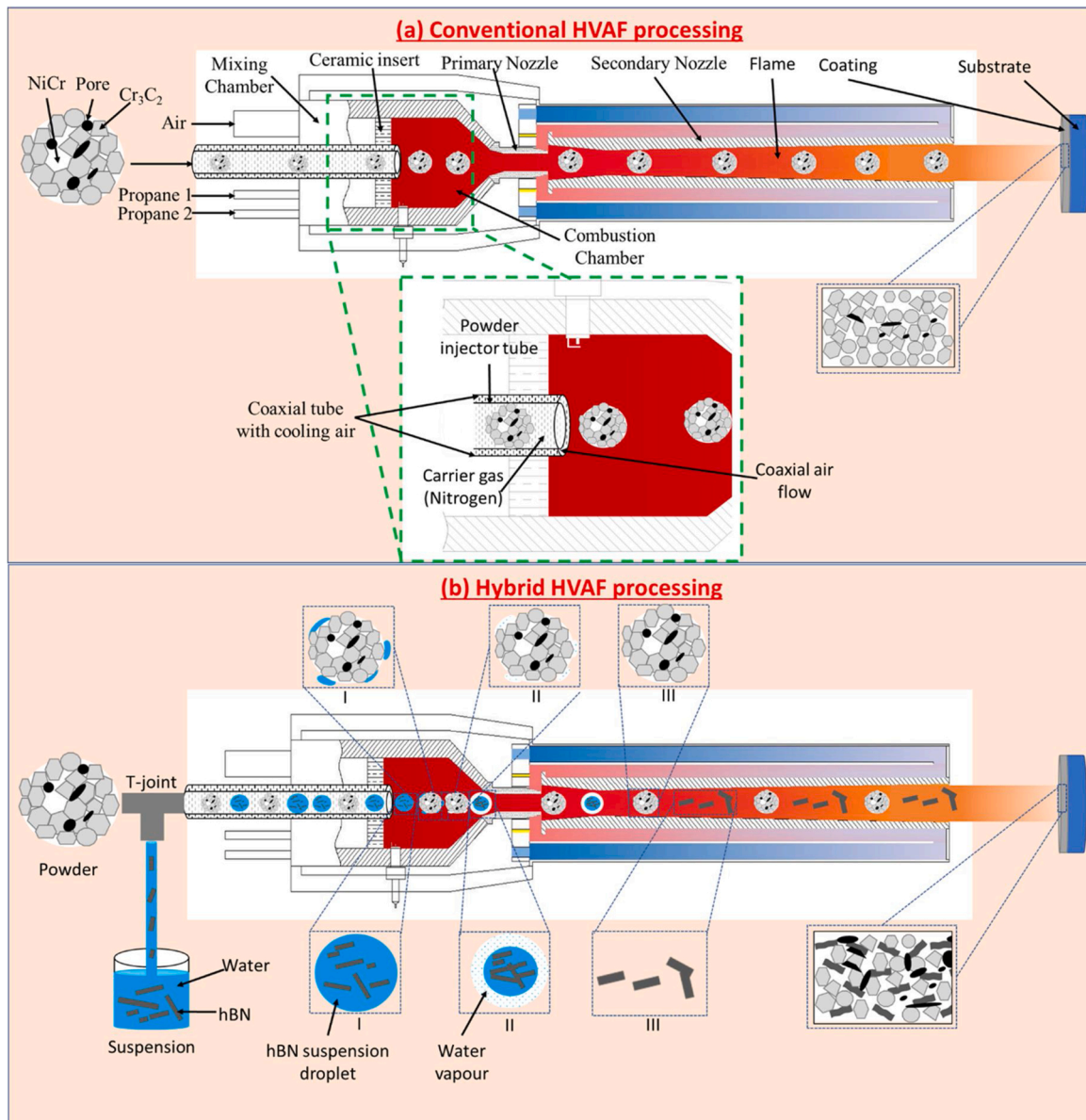


Fig. 7. Schematic of hybrid HVOF suspension-powder processing route (b) as compared to the conventional HVOF powder processing route (a).

wet  $\text{Cr}_3\text{C}_2$ -NiCr powder particles encounter a high velocity stream of gaseous combustion products in the combustion chamber due to air-fuel ignition leading to gradual evaporation of water from the suspension. This is *stage II* as shown in Fig. 7. Finally, after complete evaporation of the water, the hBN platelets as well as the dry  $\text{Cr}_3\text{C}_2$ -NiCr powder particles come in direct contact with the high velocity gas stream (termed as *stage III*) and start to heat up and partially/fully melt as well as be accelerated. The acceleration that the entrained droplets and particles achieve is extremely high in HVOF, thereby providing very little residence time in the flame before the particles impact the substrate to form coatings. The short residence time has important implications as it can prevent/suppress thermal decomposition of both the hBN as well as the  $\text{Cr}_3\text{C}_2$ -NiCr powder. Like what is shown in case of suspension plasma spraying by (Ganvir et al., 2019), it is to be noted that the above-mentioned evaporation of water from the suspension utilizes some of the available thermal energy unlike in conventional HVOF processing where there is no water evaporation. Consequently, the degree of heatup/partial melting of the particles is higher in case of conventional HVOF processing as compared to the hybrid HVOF processing route. The lower available energy in the flame in case of hybrid HVOF

processing also leads to a comparatively higher porosity and possibly weaker cohesion in the composite coating. Similar observations were made by (Mahade et al., 2020) in case of powder-suspension hybrid plasma sprayed wear resistant coatings where the hybrid coatings showed higher porosity than the traditional powder plasma sprayed coatings.

In case of the  $\text{Cr}_3\text{C}_2$ -NiCr powder particles, the NiCr matrix (melting temperature  $1455^\circ\text{C}$  (Turchi et al., 2006)) is partially/fully molten due to the flame temperature of  $\sim 1900\text{--}1950^\circ\text{C}$  (Kuroda et al., 2011) when impacting on the substrate whereas the  $\text{Cr}_3\text{C}_2$  ceramic particles (melting temperature  $\sim 1895^\circ\text{C}$  (Andersson, 1987; Chung, 2017)) do not melt and arrive in their solid state on the substrate. Similarly, the flame temperature is not enough to affect the hBN platelets (melting temperature  $\sim 3370^\circ\text{C}$ ) either, which also arrive in their solid platelet form. The hBN particles may, therefore, have less of a tendency to adhere to the solid hard  $\text{Cr}_3\text{C}_2$  ceramic particles in the coating. Consequently, it is more likely that the hBN platelets will be anchored to the partially/fully molten NiCr metal matrix or enveloped as this binder constituent plastically deforms or splats upon impact. It is also possible that the hBN platelets get entrenched in the pores formed in the coating. This is



supported by the EDS and Raman measurements shown in Figs. 5 and 6, respectively where the hBN was found at the interface of the porosity and the metal matrix. Moreover, the presence of hBN in the pores could also be a consequence of the metallographic preparation of the sample since the weak van der Waals inter-layer bond between the hBN platelets can be broken and hence the individual/few hBN platelets can be pulled out during the grinding and polishing of the sample and get entrenched in the existing coating pores or the pores formed during metallographic preparation (Du et al., 2011). In case of the composite coating, a lower deposition per pass was noted despite additional material in the form of hBN being fed along with the  $\text{Cr}_3\text{C}_2\text{-NiCr}$  powder due to the water from the suspension consuming a significant amount of thermal energy available in the combustion flame during hybrid processing.

The resultant coatings, as shown in Fig. 3, consisted of pores of various sizes and shapes, and were mainly located at the interface between the metal matrix and the ceramic carbide particles.

### 3.5. Mechanical properties

Mechanical properties of both the coatings are reported in Table 1. The hardness and fracture toughness of the traditional powder-derived coating were 1096 HV0.1 and  $5.7 \text{ MPa.m}^{0.5}$ , respectively. Whereas for the composite coating the hardness and fracture toughness values were 997 HV0.1 and  $4.0 \text{ MPa.m}^{0.5}$ , respectively. Both the hardness and fracture toughness were lower for the composite coating, however the difference in the hardness was not as obvious and significant as in fracture toughness. A significant decrease in both hardness and especially in fracture toughness of the composite coating was not surprising due to the presence of significantly higher porosity as compared to the traditional powder-derived coating. The presence of more delaminations, cracks and pores contributing to the overall porosity in the composite coating can act as stress concentrators assisting the crack initiation and propagation and hence substantially reducing the fracture toughness. Such an effect of porosity on the fracture toughness of hybrid thermal sprayed coatings is also reported in literature, for example, (Ganvir et al., 2021) and (Murray et al., 2018) showed the decrease in fracture toughness as the porosity was increased in the plasma sprayed coatings. Similarly, (Xie et al., 2017) showed the improvement in fracture toughness of the HVOF sprayed  $\text{Cr}_3\text{C}_2\text{-NiCr}$  coatings. Moreover, the incorporation of hBN into the coating could also have contributed in decreasing the fracture toughness as the inherent fracture toughness of hBN is significantly lower ( $2\text{--}3 \text{ MPa.m}^{0.5}$  (Rakib et al., 2017)) as compared to the dense  $\text{Cr}_3\text{C}_2\text{-NiCr}$  coatings ( $>4 \text{ MPa.m}^{0.5}$  (Xie et al., 2017)).

### 3.6. Sliding wear behavior

Fig. 8 (a) shows the friction coefficient at ambient condition and for different times for both the coatings. A significant reduction in the friction coefficient for the composite coating can be seen as compared to

the traditional powder-derived coating. Moreover, both the powder as well as composite coatings showed significantly lower friction coefficient (i.e. approximately 50 % lower) as compared to the traditional powder HVOF sprayed  $\text{Cr}_3\text{C}_2\text{-NiCr}$  coatings in the literature (Matikainen et al., 2017b). An interesting aspect to be noted is the behavior of the curve for both the coatings, where the traditional powder-derived coating showed stable coefficient of friction at the start of the wear test with an upward and increasing trend from about 3200 s which is attributable to the formation of abrasive media (debris) due to the wear of the coating. In contrast, in case of the composite coating the trend was increasing from the start up to 3200 s, decreased then for about 200 s before stabilizing. This behavior suggests that like the traditional powder-derived coating, abrasive media (debris) was formed in the composite coating. In fact, the sharp increasing trend at the start suggests that rather aggressive wear occurred in the initial phase of the testing in the composite coating. The early aggressive wear in the composite coating can be attributed to the weaker cohesion within the composite coating as described earlier due to the presence of higher porosity as well as substantially lower fracture toughness. However, due to the formation of the solid lubricant (hBN) film on the coating surface, the coefficient of friction was reduced despite initially aggressive wear and then stabilized for the remainder of the test. The presence of a solid lubrication film therefore avoided further wear of the coating during the sliding wear test. The average specific wear rate for both the coatings was also calculated and reported in Fig. 8(b) which shows a slightly reduced wear rate in case of the composite coating compared to the traditional powder-derived coating. The reduced average specific wear rate despite early signs of aggressive wear is due to the formation of a solid lubrication film on the surface of the composite coating which is also observed in literature by (Cao, 2016).

Post wear analysis was done by observing the 3D and 2D profiles along with SEM analysis for both the coatings. Fig. 9(a) and (b) show a section of the worn-out tracks of the traditional powder-derived and the composite coating, respectively, where the depth as well as width of the wear track can be seen to be lower for the composite coating. This can be further confirmed from the 2D plots of the wear track profiles as shown in Fig. 9(c) for both coatings. These results further suggest the presence of the solid lubricant (hBN) in the composite coating and the formation of a solid lubrication film which is beneficial for the overall wear resistance of the hybrid processed composite coating. It should be borne in mind that the difference in the mean specific wear rates between the two coatings, as shown in Fig. 8(b), can be even greater as the wear test duration is increased. This is because of stabilized wear due to the formation of solid lubrication in the composite coating and a continuously increasing wear in the traditional powder-derived coating as demonstrated by the friction coefficient plots in Fig. 8(a). However, since the scope of this work was only limited to demonstrating a successful incorporation of a solid lubricant in the form of a suspension using HVOF process, wear tests for longer duration were not conducted.

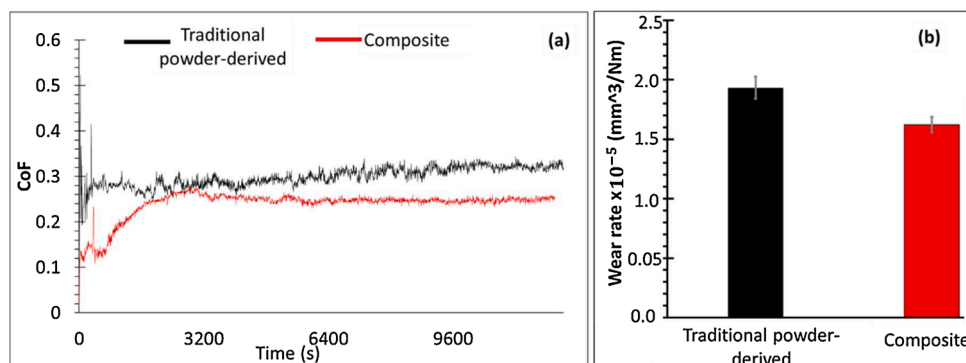
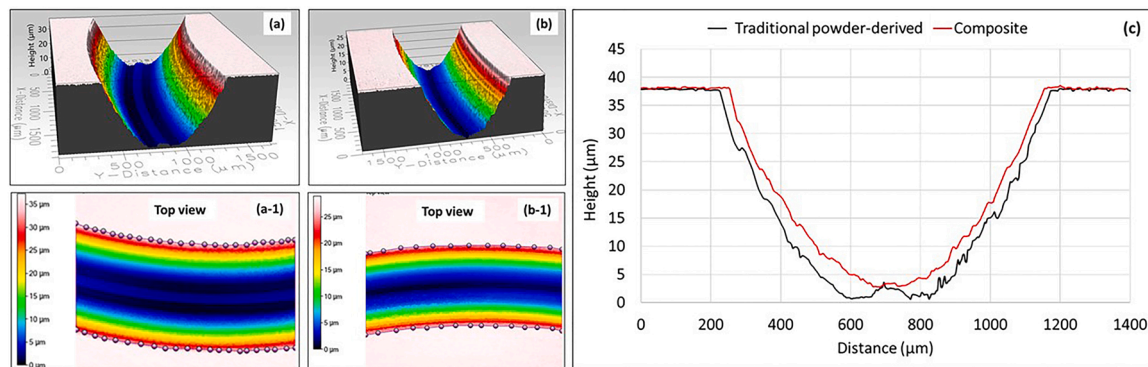
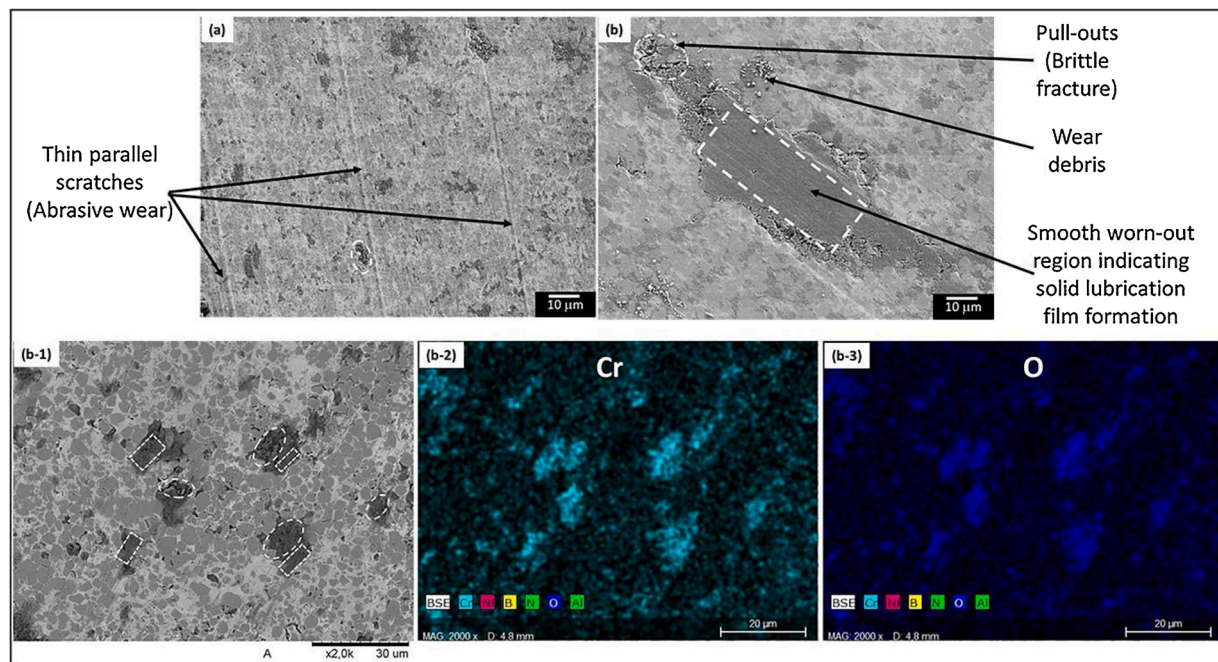


Fig. 8. Coefficient of friction (a) and specific wear rate (b) measured after sliding wear test shown for both the coatings studied in this work.



**Fig. 9.** 3D profile plots (a and b) as well as the top view (a-1 and b-1) for a section of one of the wear tracks for both the traditional powder-derived and the composite coatings, respectively studied in this work and their corresponding 2D profile (c).



**Fig. 10.** SEM micrographs of wear tracks for (a) traditional powder-derived and (b and b-1) composite coatings along with the (b-3 & b-4) EDS analysis of the entire region of micrograph (b-1) showing the presence of Chromium and Oxygen in the darker regions (as marked by the white dotted rectangles and ellipses).

### 3.6.1. Post wear analysis

To better understand the wear behavior, the wear tracks of both the coatings were investigated by use of SEM and the resultant micrographs are shown in Fig. 10. Both coatings showed wear scars; the traditional powder-derived coating shows severe long and thin parallel scratches but no major pull-outs, whereas the composite coating can be seen to be covered with a lot of wear debris and shows also the presence of sever pull-outs spread across the whole wear track. The large number of thin parallel scratches indicates that the abrasive wear is an important wear mechanism using hard metal as the countersurface, whereas the large pull-outs formed in the wear tracks encircled in Fig. 10 are attributed to the typical brittle fracture wear mechanism (Guilemany et al., 2002).

Although both the coatings showed a mixture of the two wear mechanisms, as can be seen from Fig. 10(a) and Fig. 10(b and b-1), the extent of brittle fracture was higher in the composite coating as compared to the traditional powder-derived coating where an abrasive wear mechanism was dominant. Moreover, both the coatings also showed the presence of darker regions in the wear track which was not observed in the as-sprayed coatings. The EDS analysis confirmed that the darker regions were consisting of Cr (Fig. 10(b-2)) and O (Fig. 10(b-3))

indicating that the worn surface was oxidized with primarily the presence of chromium oxide. Another important observation from Fig. 10 (b and b-1) was the formation of smooth worn-out surfaces in the composite coating indicating formation of a solid lubrication film as marked by the white dotted rectangles. Similar observations were also made and described in literature where the addition of hBN in a  $\text{Cr}_3\text{C}_2$ -NiCr coating showed formation of a solid lubricating film when performing a ball-on-disc wear test (Cao, 2016). As shown from the SE micrographs in Fig. 11, a solid lubrication film is also observed on the wear scar of the alumina counter-body in contact with the composite coating. The tribo-film is not observed on the wear scar of the alumina ball in contact with the powder-derived coatings, see Fig. 11a. Here, the wear scar is characterized with the presence of adherent wear debris.

Raman analysis was also performed on the oxides formed along the wear track of the composite coating and the results are shown in Fig. 12. The Raman peaks observed in the range of  $300$  to  $600\text{ cm}^{-1}$  correspond to the presence of  $\text{Cr}_2\text{O}_3$  (Liu et al., 2019; Matikainen et al., 2017b), whereas the peak at around  $680\text{ cm}^{-1}$  can be related to the  $\text{NiCr}_2\text{O}_4$  phase (Hosterman et al., 2013). The small and broad peak observed at around  $1360\text{ cm}^{-1}$  can be associated to hBN. As compared to the Raman



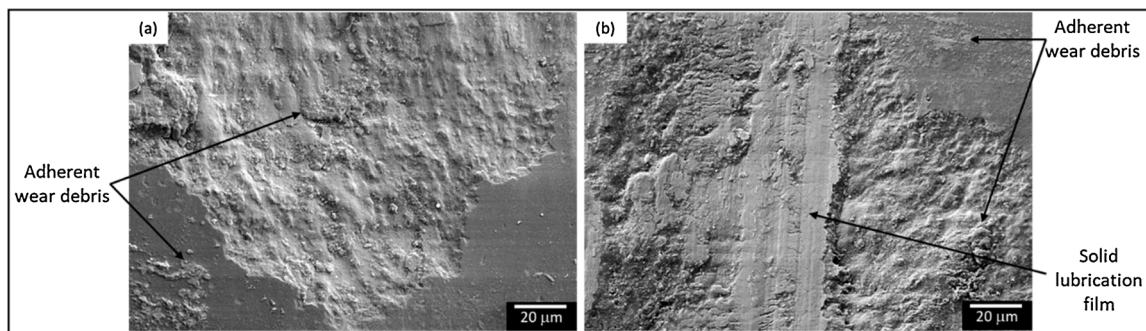


Fig. 11. SE micrographs of the wear scars produced on the alumina counter-body in contact with the powder-derived coating (a) and the composite coating (b).

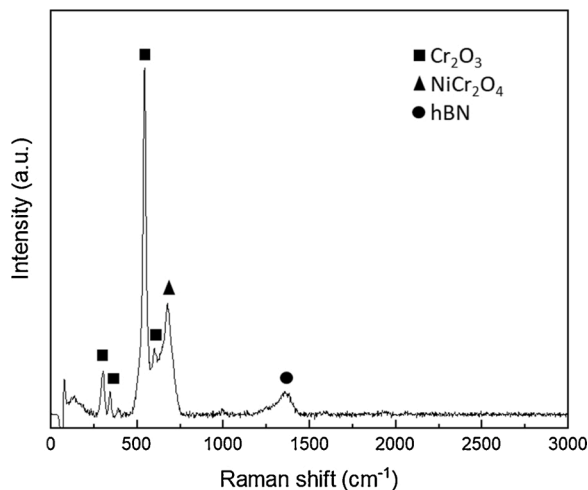


Fig. 12. Raman spectrum acquired from the wear track of the composite coating.

spectra acquired from the composite coating (see Fig. 6), the hBN peak shown in Fig. 12 appears broader and it is slightly shifted toward lower Raman shifts. Strain in hBN structure formed as a consequence of the wear test can be held responsible of the observed shift and broadening of the hBN Raman peak (Gorbachev et al., 2011). Furthermore, the prominent intensity of the oxide peaks, as compared to the intensity of the hBN, could suggest that the hBN in the wear track is covered by the formed tribo-oxides. To confirm this hypothesis FIB lamellae extracted from the tribo-oxides in the wear track will be analysed in a forthcoming work.

The reason for extensive brittle fracture wear in the composite coating was, as explained before, the higher coating porosity leading to lower hardness and significantly lower fracture toughness than in the traditional powder-derived coating. The weaker cohesion in the

composite coating due to the presence of higher porosity can result in easy material removal due to brittle fracture which can pull the ceramic carbide particles out of the metal matrix, as shown in the schematic in Fig. 13. The harder ceramic carbide particles can further damage the coating due to the abrasion between ball, debris and coating leading to excessive wear at the start of the wear test. However, as schematically shown in Fig. 13, during material removal, hBN platelets are also removed and mixed with the rest of the debris. After several wear cycles, the hBN platelets can form a continuous solid lubricating film between the ball and the coating. This is also the reason that the friction coefficient of the composite coating stabilizes after some time as already explained and, therefore, the overall wear rate was lower despite of higher porosity and lower mechanical properties.

It is important to point out that this was the first attempt by the authors to deposit hBN reinforced  $\text{Cr}_3\text{C}_2$ -NiCr coating via hybrid suspension-powder route using HVAF process. The sole aim was to demonstrate the successful incorporation of hBN in the cermet matrix. The porosity in the composite coating can be substantially minimized if the HVAF process is further optimized for such coatings by increasing the torch power so that there is enough energy in the flame to better melt the metal matrix and avoid the formation of porosity. The hybrid composite coatings deposited after optimization should be able to further reduce the wear and increase the difference in wear resistance between the composite and the traditional powder-derived coating, in particular the early damage caused due to the brittle fracture could then be largely minimized.

#### 4. Future developments to process liquid feedstock in HVAF

It is important to point out that the existing suspension feeding system used for this preliminary study utilizing a suspension in an HVAF system needs further improvement to stabilize the suspension flow through the injector. The existing feeder was based on a two-roller peristaltic pump which exhibits pulsation at the outlet due to the extremely high backpressure in an HVAF system. While the present

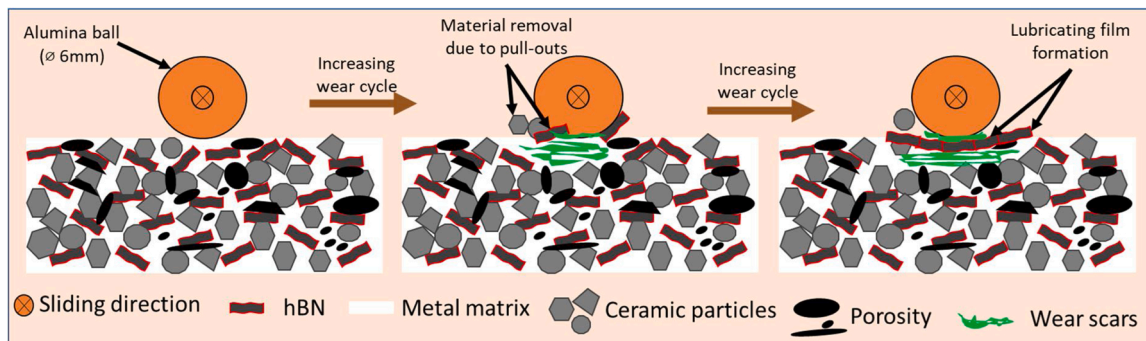


Fig. 13. A schematic showing the wear mechanism in the hybrid processed composite coating and the formation of a solid lubrication film.



feeding system/pump has a gas accumulator that acts as a pulsation damper, this damper system is typically tuned for feeding suspensions through a plasma spray torch that has a back pressure to the pump of 10 Psi. Using the same with the HVOF torch that gives a back pressure of 100 Psi results in a significant mismatch and compromises its damping capability. The resulting pulsation can result in non-uniform injection of the hBN suspension. In future work, the authors will try to modify the feeding set-up to overcome such a pulsation effect.

## 5. Conclusions

For the first time, this work has successfully demonstrated incorporation of a 2D material i.e., hBN into a  $\text{Cr}_3\text{C}_2$ -NiCr cermet matrix, using the emerging HVOF technology via hybrid suspension-powder route. The tribological performance of the hybrid powder-suspension composite coating was assessed by a ball-on disc wear test and compared to that of the traditional powder-derived  $\text{Cr}_3\text{C}_2$ -NiCr coating which was deposited using the traditional powder spraying approach. Despite of higher porosity, lower hardness and lower fracture toughness, the composite coating showed improved wear performance compared to the traditional powder-derived coating. The increased porosity in the composite coating was attributed to the availability of less energy from the flame during the deposition of the composite coating, since a substantial amount of flame energy was consumed in the evaporation of the solvent from the hBN suspension, which resulted in insufficient melting of the metal matrix. The improved wear performance of the composite coating was due to the formation of a solid lubrication film. The primary wear mechanism in the composite coating was brittle fracture along with an abrasive wear mechanism. Further optimization of the HVOF process parameters for the simultaneous deposition of hybrid powder-suspension by increasing the flame energy can further improve the wear performance by reducing the porosity and increasing the coating hardness and fracture toughness.

## Data availability

The raw/processed data required to reproduce these findings will be made available on request.

## CRediT authorship contribution statement

**Ashish Ganvir:** Analysis of all the results & Writing-Original draft of manuscript. **Adwait Rajeev Jahagirdar:** Metallographic preparation & microstructural characterization, Mechanical & Wear testing Antonio Mulone, High magnification SEM imaging and analysis, Raman & EDS experiments and analysis, Review & editing. **Louise Örnfeldt:** Metallographic preparation & microscopy. **Stefan Björklund:** Engineering liquid feedstock delivery in HVOF spraying, coating deposition, Review & editing. **Uta Klement:** Supervision in SEM and RAMAN analysis, Review & editing, Resources, Funding acquisition. **Shrikant Joshi:** Conceptualization, Validation, Review & editing, Resources, Funding acquisition, Project administration & execution

## Declaration of Competing Interest

The authors report no declarations of interest.

## Acknowledgements

The authors are grateful for financial support from the Knowledge Foundation, Sweden through the project HiPerCOAT (Dnr. 20180197). Additionally, U. Klement and A. Mulone also thank the Area of Advance Production at Chalmers University of Technology for financial support. Sincere thanks to Dr. Y. Yao (Chalmers University of Technology) for assistance with imaging the hBN.

## References

- Andersson, J.-O., 1987. Thermodynamic properties of Cr-C. *Calphad* 11, 271–276. [https://doi.org/10.1016/0364-5916\(87\)90045-9](https://doi.org/10.1016/0364-5916(87)90045-9).
- ASTM G99 - Standard Test Method for Wear Testing with a Pin-on-Disk Apparatus | Engineering360 [WWW Document], n.d. URL <https://standards.globalspec.com/std/10072001/ASTM%20G99> (accessed 7.4.20).
- Björklund, S., Goel, S., Joshi, S., 2018. Function-dependent coating architectures by hybrid powder-suspension plasma spraying: injector design, processing and concept validation. *Mater. Des.* 142, 56–65. <https://doi.org/10.1016/j.matdes.2018.01.002>.
- Cao, Y., 2016. Effects of hBN content on the microstructure and properties of atmospheric plasma-sprayed NiCr/Cr<sub>3</sub>C<sub>2</sub>-hBN composite coatings. *J. Therm. Spray Technol.* <https://doi.org/10.1007/s11666-016-0385-9>.
- Chhabra, P., Kaur, M., 2020. Elevated-temperature wear study of HVOF spray Cr<sub>3</sub>C<sub>2</sub>-NiCr-Coated die steels. *J. Tribol.* 142 <https://doi.org/10.1115/1.4046017>.
- Chkhartishvili, L., Nackebia, G.T.D., Bzhilava, T., Kalandadze, I., 2016. Hexagonal Boron Nitride As A Solid Lubricant Additive (An Overview), p. 9.
- Chung, D.D.L., 2017. 7 - carbon-matrix composites. In: Chung, D.D.L. (Ed.), *Carbon Composites* (Second Edition). Butterworth-Heinemann, pp. 387–466. <https://doi.org/10.1016/B978-0-12-804459-9.00007-5>.
- Donnet, C., Erdemir, A., 2004. Historical developments and new trends in tribological and solid lubricant coatings. *Surf. Coat. Technol. Proceedings of Symposium G on Protective Coatings and Thin Films-03, of the E-MRS 2003 Spring Conference*, pp. 76–84. <https://doi.org/10.1016/j.surfcoat.2003.10.022>.
- Du, L., Huang, C., Zhang, W., Li, T., Liu, W., 2011. Preparation and wear performance of NiCr/Cr<sub>3</sub>C<sub>2</sub>-NiCr/hBN plasma sprayed composite coating. *Surf. Coat. Technol.* 205, 3722–3728. <https://doi.org/10.1016/j.surfcoat.2011.01.031>.
- Espallargas, N., Armada, S., 2015. A new type of self-lubricated thermal spray coatings: liquid lubricants embedded in a metal matrix. *J. Therm. Spray Technol.* 24, 222–234. <https://doi.org/10.1007/s11666-014-0152-8>.
- Espallargas, N., Berget, J., Guilemany, J.M., Benedetti, A.V., Suegama, P.H., 2008. Cr<sub>3</sub>C<sub>2</sub>-NiCr and WC-Ni thermal spray coatings as alternatives to hard chromium for erosion-corrosion resistance. *Surf. Coat. Technol.* 202, 1405–1417. <https://doi.org/10.1016/j.surfcoat.2007.06.048>.
- Evans, A.G., Willshaw, T.R., 1976. Quasi-static solid particle damage in brittle solids—I. Observations analysis and implications. *Acta Metall.* 24, 939–956. [https://doi.org/10.1016/0001-6160\(76\)90042-0](https://doi.org/10.1016/0001-6160(76)90042-0).
- Forn, A., Picas, J.A., Simón, M.J., 2003. Mechanical and tribological properties of Al-Si-Mo plasma-sprayed coatings. *J. Mater. Process. Technol.* 2001 (143–144), 52–57. [https://doi.org/10.1016/S0924-0136\(03\)00318-2](https://doi.org/10.1016/S0924-0136(03)00318-2).
- Ganvir, A., 2016. Microstructure and Thermal Conductivity of Liquid Feedstock Plasma Sprayed Thermal Barrier Coatings. *DIVA*.
- Ganvir, A., Vaidhyanathan, V., Markocsan, N., Gupta, M., Pala, Z., Lukac, F., 2018. Failure analysis of thermally cycled columnar thermal barrier coatings produced by high-velocity-air fuel and axial-suspension-plasma spraying: a design perspective. *Ceram. Int.* 44, 3161–3172. <https://doi.org/10.1016/j.ceramint.2017.11.084>.
- Ganvir, A., Calinas, R.F., Markocsan, N., Curry, N., Joshi, S., 2019. Experimental visualization of microstructure evolution during suspension plasma spraying of thermal barrier coatings. *J. Eur. Ceram. Soc.* 39, 470–481. <https://doi.org/10.1016/j.jeurceramsoc.2018.09.023>.
- Ganvir, A., Goel, S., Govindarajan, S., Jahagirdar, A.R., Björklund, S., Klement, U., Joshi, S., 2021. Tribological performance assessment of Al<sub>2</sub>O<sub>3</sub>-YSZ composite coatings deposited by hybrid powder-suspension plasma spraying. *Surf. Coat. Technol.* <https://doi.org/10.1016/j.surfcoat.2021.126907>, 126907.
- Göncü, Y., Geçgin, M., Bakan, F., Ay, N., 2017. Electrophoretic deposition of hydroxyapatite-hexagonal boron nitride composite coatings on Ti substrate. *Mater. Sci. Eng. C* 79, 343–353. <https://doi.org/10.1016/j.msec.2017.05.023>.
- Gorbachev, R.V., Riaz, I., Nair, R.R., Jalil, R., Britnell, L., Belle, B.D., Hill, E.W., Novoselov, K.S., Watanabe, K., Taniguchi, T., Geim, A.K., Blake, P., 2011. Hunting for monolayer boron nitride: optical and raman signatures. *Small* 7, 465–468. <https://doi.org/10.1002/sml.201001628>.
- Guilemany, J.M., Miguel, J.M., Vizcaino, S., Lorenzana, C., Delgado, J., Sánchez, J., 2002. Role of heat treatments in the improvement of the sliding wear properties of Cr<sub>3</sub>C<sub>2</sub>-NiCr coatings. *Surf. Coat. Technol.* 157, 207–213. [https://doi.org/10.1016/S0257-8972\(02\)00148-2](https://doi.org/10.1016/S0257-8972(02)00148-2).
- Guo, X., Planche, M.-P., Chen, J., Liao, H., 2014. Relationships between in-flight particle characteristics and properties of HVOF sprayed WC-CoCr coatings. *J. Mater. Process. Technol.* 214, 456–461. <https://doi.org/10.1016/j.jmatprotec.2013.09.029>.
- Hoornaert, T., Hua, Z.K., Zhang, J.H., 2010. Hard wear-resistant coatings: a review. In: Luo, J., Meng, Y., Shao, T., Zhao, Q. (Eds.), *Advanced Tribology*. Springer, Berlin, Heidelberg, pp. 774–779. [https://doi.org/10.1007/978-3-642-03653-8\\_257](https://doi.org/10.1007/978-3-642-03653-8_257).
- Hosterman, B.D., Farley, J.W., Johnson, A.L., 2013. Spectroscopic study of the vibrational modes of magnesium nickel chromite, Mg<sub>9</sub>Ni<sub>1</sub>-xCr<sub>2</sub>O<sub>4</sub>. *J. Phys. Chem. Solids* 74, 985–990. <https://doi.org/10.1016/j.jpcs.2013.02.017>.
- Huang, C., Du, L., Zhang, W., 2009. Effects of solid lubricant content on the microstructure and properties of NiCr/Cr<sub>3</sub>C<sub>2</sub>-BaF<sub>2</sub>-CaF<sub>2</sub> composite coatings. *J. Alloys. Compd.* 479, 777–784. <https://doi.org/10.1016/j.jallcom.2009.01.062>.
- ImageJ Software [WWW Document], n.d. Image Process. Anal. Java. <http://imagej.nih.gov/ij/> (accessed 11.17.14).
- Janka, L., Norpoth, J., Trache, R., Thiele, S., Berger, L.-M., 2017. HVOF- and HVOF-Sprayed Cr<sub>3</sub>C<sub>2</sub>-NiCr coatings deposited from feedstock powders of spherical morphology: microstructure formation and high-stress abrasive wear resistance up to 800 °C. *J. Therm. Spray Technol.* 26, 1720–1731. <https://doi.org/10.1007/s11666-017-0621-y>.
- Kerkwijk, B., García, M., van Zyl, W.E., Winnubst, L., Mulder, E.J., Schipper, D.J., Verweij, H., 2004. Friction behaviour of solid oxide lubricants as second phase in

- $\alpha$ -Al<sub>2</sub>O<sub>3</sub> and stabilised ZrO<sub>2</sub> composites. *Wear* 256, 182–189. [https://doi.org/10.1016/S0043-1648\(03\)00388-0](https://doi.org/10.1016/S0043-1648(03)00388-0).
- Kiilakoski, J., Puranen, J., Heinonen, E., Koivuluoto, H., Vuoristo, P., 2019. Characterization of powder-precursor HVOF-Sprayed Al<sub>2</sub>O<sub>3</sub>-YSZ/ZrO<sub>2</sub> coatings. *J. Therm. Spray Technol.* 28, 98–107. <https://doi.org/10.1007/s11666-018-0816-x>.
- Kuroda, S., Watanabe, M., Kim, K., Katanoda, H., 2011. Current status and future prospects of warm spray technology. *J. Therm. Spray Technol.* 20, 653–676. <https://doi.org/10.1007/s11666-011-9648-7>.
- Lima, C.R.C., Belém, M.J.X., Fals, H.D.C., Rovere, C.A.D., 2020. Wear and corrosion performance of Stellite 6® coatings applied by HVOF spraying and GTAW hotwire cladding. *J. Mater. Process. Technol.* 284, 116734 <https://doi.org/10.1016/j.jmatprotec.2020.116734>.
- Liu, Q., Bai, Y., Wang, H.D., Ma, G.Z., Liu, M., Chu, C.Y., Sun, Y.W., Fan, W., Ding, F., Zhao, B., Wang, Y.T., 2019. Microstructural evolution of carbides and its effect on tribological properties of SAPS or HVOF sprayed NiCr–Cr<sub>3</sub>C<sub>2</sub> coatings. *J. Alloys. Compd.* 803, 730–741. <https://doi.org/10.1016/j.jallcom.2019.06.291>.
- Liu, X., Zhao, X., Yang, F., 2020. Room-temperature and high-temperature wear behaviors of As-Sprayed and annealed Cr<sub>3</sub>C<sub>2</sub>-25NiCr coatings prepared by high velocity air-fuel spraying. *Coatings* 10, 1090. <https://doi.org/10.3390/coatings10111090>.
- Lu, H., Shang, J., Jia, X., Li, Y., Li, F., Li, J., Nie, Y., 2020. Erosion and corrosion behavior of shrouded plasma sprayed Cr<sub>3</sub>C<sub>2</sub>-NiCr coating. *Surf. Coat. Technol.* 388 <https://doi.org/10.1016/j.surfcoat.2020.125534>, 125534.
- Mahade, S., Björklund, S., Govindarajan, S., Olsson, M., Joshi, S., 2020. Novel wear resistant carbide-laden coatings deposited by powder-suspension hybrid plasma spray: characterization and testing. *Surf. Coat. Technol.* 399, 126147 <https://doi.org/10.1016/j.surfcoat.2020.126147>.
- Matikainen, V., Bolelli, G., Koivuluoto, H., Honkanen, M., Vippola, M., Lusvarghi, L., Vuoristo, P., 2017a. A study of Cr<sub>3</sub>C<sub>2</sub>-Based HVOF- and HVAF-Sprayed coatings: microstructure and carbide retention. *J. Therm. Spray Technol.* 26, 1239–1256. <https://doi.org/10.1007/s11666-017-0578-x>.
- Matikainen, V., Bolelli, G., Koivuluoto, H., Sassatelli, P., Lusvarghi, L., Vuoristo, P., 2017b. Sliding wear behaviour of HVOF and HVAF sprayed Cr<sub>3</sub>C<sub>2</sub>-based coatings. *Wear. NORDTRIB 2016: The 17th Nordic Symposium on Tribology* 57–71. <https://doi.org/10.1016/j.wear.2017.04.001>, 388–389.
- Matthews, S., James, B., Hyland, M., 2009. The role of microstructure in the high temperature oxidation mechanism of Cr<sub>3</sub>C<sub>2</sub>-NiCr composite coatings. *Corros. Sci.* 51, 1172–1180. <https://doi.org/10.1016/j.corsci.2009.02.027>.
- Motru, S., Hussain, N., Ali Khan, Z., Avinash, 2020. Tribological studies of high surface finish ceramic coatings for low friction and adhesive wear resistant applications. *Mater. Today Proc.* 2019 (27), 2208–2212. <https://doi.org/10.1016/j.matpr.2019.09.098>.
- Murray, J.W., Leva, A., Joshi, S., Hussain, T., 2018. Microstructure and wear behaviour of powder and suspension hybrid Al<sub>2</sub>O<sub>3</sub>-YSZ coatings. *Ceram. Int.* 44, 8498–8504. <https://doi.org/10.1016/j.ceramint.2018.02.048>.
- Rakib, T., Mojumder, S., Das, S., Saha, S., Motalab, M., 2017. Graphene and its elemental analogue: a molecular dynamics view of fracture phenomenon. *Phys. B Condens. Matter* 515, 67–74. <https://doi.org/10.1016/j.physb.2017.04.009>.
- Shtansky, D.V., Bondarev, A.V., Kiryukhantsev-Korneev, Ph.V., Rojas, T.C., Godinho, V., Fernández, A., 2013. Structure and tribological properties of MoCN-Ag coatings in the temperature range of 25–700°C. *Appl. Surf. Sci.* 273, 408–414. <https://doi.org/10.1016/j.apsusc.2013.02.055>.
- Tsunekawa, Y., Ozdemir, I., Okumiya, M., 2006. Plasma sprayed cast iron coatings containing solid lubricant graphite and h-BN structure. *J. Therm. Spray Technol.* 15, 239–245. <https://doi.org/10.1361/105996306X108156>.
- Turchi, P.E.A., Kaufman, L., Liu, Z.-K., 2006. Modeling of Ni–Cr–Mo based alloys: part I—phase stability. *Calphad* 30, 70–87. <https://doi.org/10.1016/j.calphad.2005.10.003>.
- Umanskii, A.P., Terentiev, A.E., Brazhevsky, V.P., Chernyshov, A.A., Labunets, V.F., Radko, O.V., Zakiev, I.M., 2020. Wear resistance of plasma-sprayed coatings in intensive abrasive wear conditions. *Powder Metall. Met. Ceram.* 58, 559–566. <https://doi.org/10.1007/s11106-020-00110-3>.
- Urbonaite, S., Hälldahl, L., Svensson, G., 2008. Raman spectroscopy studies of carbide derived carbons. *Carbon* 46, 1942–1947. <https://doi.org/10.1016/j.carbon.2008.08.004>.
- Varis, T., Suhonen, T., Laakso, J., Jokipii, M., Vuoristo, P., 2020. Evaluation of Residual Stresses and Their Influence on Cavitation Erosion Resistance of High Kinetic HVOF and HVAF-Sprayed WC-CoCr Coatings. *J. Therm. Spray Technol.* 29, 1365–1381. <https://doi.org/10.1007/s11666-020-01037-2>.
- Verstak, A., Kusinski, G., 2012. High-velocity air-fuel spraying and its applications in oil and gas industry. Presented at the Proceedings of the International Thermal Spray Conference.
- Wang, H., Qiu, Q., Gee, M., Hou, C., Liu, X., Song, X., 2020. Wear resistance enhancement of HVOF-sprayed WC-Co coating by complete densification of starting powder. *Mater. Des.* 191, 108586 <https://doi.org/10.1016/j.matdes.2020.108586>.
- Xie, M., Lin, Y., Ke, P., Wang, S., Zhang, S., Zhen, Z., Ge, L., 2017. Influence of process parameters on high velocity oxy-fuel sprayed Cr<sub>3</sub>C<sub>2</sub>-25%NiCr coatings. *Coatings* 7, 98. <https://doi.org/10.3390/coatings7070098>.
- Xiong, W., Ma, M., Zhang, J., Lian, Y., 2020. The effects of Cr<sub>2</sub>O<sub>3</sub> particles on the microstructure and wear-resistant properties of electrodeposited CoNiP coatings. *Surf. Coat. Technol.* 381, 125167 <https://doi.org/10.1016/j.surfcoat.2019.125167>.
- Zhang, L., Hou, J.B., 2013. Study of microstructure and phase of plasma sprayed Cr<sub>3</sub>C<sub>2</sub>-NiCr coating before and after the sparking plasma sintering. *Phys. Proced.* 50, 293–296. <https://doi.org/10.1016/j.phpro.2013.11.047>.
- Zhang, Xiao-feng, Zhang, Xiang-lin, Wang, A., Huang, Z., 2009. Microstructure and properties of HVOF sprayed Ni-based submicron WS<sub>2</sub>/CaF<sub>2</sub> self-lubricating composite coating. *Trans. Nonferrous Met. Soc. China* 19, 85–92. [https://doi.org/10.1016/S1003-6326\(08\)60233-2](https://doi.org/10.1016/S1003-6326(08)60233-2).
- Zhu, X., Wei, X., Huang, Y., Wang, F., Yan, P., 2019. High-Temperature Friction and Wear Properties of NiCr/hBN Self-Lubricating Composites. <https://doi.org/10.3390/MET9030356>.